In R. A. Adey *et al.*, eds., *Simulation and Design of Microsystems and Microstructures* (Proceedings of the 1st International Conference on Simulation and Design of Microsystems and Microstructures), Computational Mechanics Publications, Southampton, U.K., 1995, pp. 175-183.

Modelling and simulation of microresonators with meander suspensions

G. K. Fedder, K. H. Clark
Department of Electrical and Computer Engineering and the Robotics Institute, Carnegie Mellon University, Pittsburgh, Pennsylvania 15213-3890 U.S.A.

Abstract

Surface-micromachined comb-drive resonators suspended by meander springs are modelled and simulated. General analytic expressions for lateral spring constants and effective mass of meander springs are derived and verified by finite-element simulations. The spring constant equations are accurate to within 1% over a wide range of geometries. Analytic, simulated, and measured resonant frequency values agree to within 0.3% for each of ten different microresonator designs.

1 Introduction

Surface-micromachined structures have been adopted as the mechanical elements in a variety of integrated microsystems, such as polysilicon microaccelerometers, microresonator transducers, and active micromirror displays. Currently, these microstructures are handcrafted in a physical layout and analyzed using electromechanical and mechanical finite-element simulation. In contrast to the finite-element analysis approach, we view microelectromechanical design in much the same way that circuit design is accomplished: as a process of assembling and sizing components to meet system specifications. Parameterized models of micromechanical components are required in order to simulate microsystems at this higher level of abstraction. The present lack of component models for specific micromechanical process technologies represents a barrier to optimal design of integrated microsystems. We have chosen microresonators as an application vehicle to demonstrate our general approach to micromechanical modelling and simulation.

Previous component modelling for microresonators includes lateral viscous damping by Zhang [1] and electrostatic force of comb-finger actuators by

Johnson [2]. Small-signal equivalent circuits for microresonators operating at or near resonance have been developed (e.g. Nguyen [3]). In this paper, we focus on the modeling of meander springs for simulations of microresonators under arbitrary operating conditions. Meander springs have been designed in compact ultra-compliant suspensions for x-y micropositioners (e.g. Zhang [4]), multi-mode positioners (e.g. Fedder [5]), and optical microshutters (e.g. Jaeklin [6]). Meander suspensions have spring constants that are linear over a relatively large displacement and are less sensitive to residual stress than straight-beam fixed-fixed suspensions. The lumped-parameter analytic models allow the microsystem designer to analyze trade-offs quickly and to size the suspension appropriately through accurate and efficient simulation.

In the following sections, analytic equations for the lateral spring constants and effective mass of the meander suspension are derived. To verify the expressions, the analytic results are compared with finite-element simulations and experimental measurements for a set of ten lateral microresonators.

2 Modelling of Meander Springs

A. Resonator Description

The lateral microresonators are fabricated using a four-mask surface-micromachining polysilicon process (e.g. Tang [7]). A scanning electron micrograph of a lateral resonator suspended by four meander springs is shown in Figure 1. Two comb-finger electrostatic actuators are situated symmetrically on two sides of the rigid shuttle mass. Each comb drive has 16 fingers on the shuttle side of the comb. Small anchors are placed inside the shuttle frame to act as lateral-displacement limit stops. Other physical parameters for the microresonators are given in section 3.

B. Meander Spring Constants

A schematic of one spring is shown in Figure 2. Each meander is of length *a*, and width *b*, except for the first and last meanders, which are of width *c*. We call

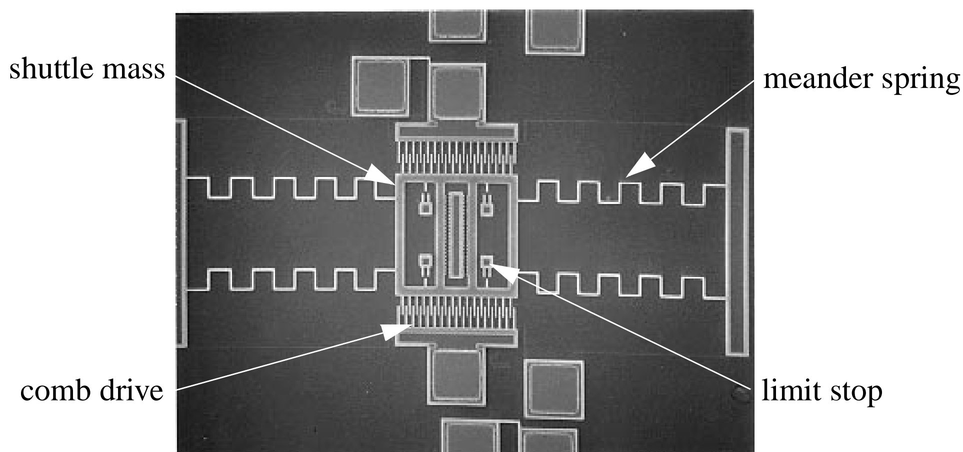

Figure 1. Scanning electron micrograph of a lateral microresonator suspended by four meander springs.

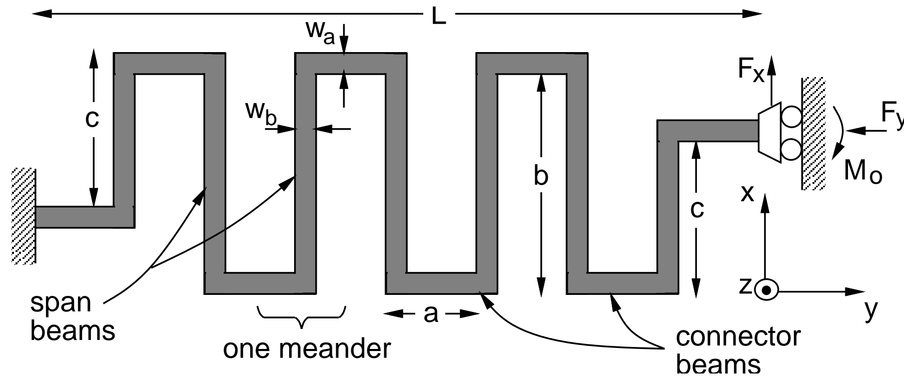

Figure 2. Meander spring schematic with guided-end boundary condition.

the beam segments that span the meander width span beams (or spans) and the beam segments that connect the spans are called connector beams (or connectors). We only consider the case where all spans are equal (*b*=*c*). However, the analysis can be easily extended to the general case. Because of the flexure symmetry in the suspension, the end of the spring has a guided-end boundary condition, where only translation in the preferred *x*-direction is allowed. The reaction forces are F_x and F_y and the couple is M_o at the ends of the spring.

In the following analysis, the spring constants are derived using energy methods (Timoshenko [8]). The strain energy from each beam segment of the spring is summed to obtain the total strain energy,

$$U = \sum_{i=1}^{n} \int_0^a \frac{M_{a,i}^2}{2EI_a}\, d\xi + \sum_{j=1}^{n-1} \int_0^b \frac{M_{b,j}^2}{2EI_b}\, d\xi \tag{1}$$

where *n* is the number of meanders, *E* is Young's modulus, I_a and I_b are the bending moments of inertia for the connectors and spans, respectively, $M_{a,i}$ is the moment of the ith connector, and $M_{b,j}$ is the moment of the jth span, where *i*=*j*=1 at the guided-end of the spring. The moments of the beam segments are deduced from a free-body diagram of the spring. When determining the *x*-directed spring constant, displacement of the spring end in the *y*-direction (δy) and rotation of the spring end (θ_o) are constrained to be zero while the displacement in the *x*-direction (δx) is unconstrained. Application of Castigliano's second theorem produces three equations in three unknown variables (F_x, M_o, and δx).

$$\delta_y = \frac{\partial U}{\partial F_y} = 0 \tag{2}$$

$$\theta_o = \frac{\partial U}{\partial M_o} = 0 \tag{3}$$

$$\delta_x = \frac{\partial U}{\partial F_x} \tag{4}$$

The solution to eqns (2)-(4) results in a closed-form expression for the x-directed spring constant of the fixed-fixed meander suspension, which is given by $k_x = 4\, F_x / \delta x$.

$$k_x = \begin{cases} \dfrac{48EI_b\left[(3\tilde{a}+b)n-b\right]}{a^2n\left[(3\tilde{a}^2+4\tilde{a}b+b^2)n^3-2b(5\tilde{a}+2b)n^2+(5b^2+6\tilde{a}b-9\tilde{a}^2)n-2b^2\right]} & ;n \text{ even} \\ \dfrac{48EI_b}{a^2n\left[(\tilde{a}+b)n^2-3bn+2b\right]} & ;n \text{ odd} \end{cases} \quad (5)$$

where $\tilde{a} = (I_b / I_a)\, a$. A similar procedure yields the y-directed spring constant, but in this case $\delta x = 0$, $\theta_o = 0$, and δy is unconstrained.

$$k_y = \begin{cases} \dfrac{48EI_b\left[(\tilde{a}+b)n^2-3bn+2b\right]}{b^2\left[(3\tilde{a}^2+4\tilde{a}b+b^2)n^3-2b(5\tilde{a}+2b)n^2+(5b^2+6\tilde{a}b-9\tilde{a}^2)n-2b^2\right]} & ;n \text{ even} \\ \dfrac{48EI_b\left[(\tilde{a}+b)n-b\right]}{b^2(n-1)\left[(3\tilde{a}^2+4\tilde{a}b+b^2)n+3\tilde{a}^2-b^2\right]} & ;n \text{ odd} \end{cases} \quad (6)$$

Simplified approximations for (5)-(6) can be found for large n, which is defined as $n >> 3\, b / (\tilde{a} + b)$.

$$k_x \approx \frac{48EI_b}{a^2(\tilde{a}+b)n^3} \quad (7)$$

$$k_y \approx \frac{48EI_b}{b^2(3\tilde{a}+b)n} \quad (8)$$

The lateral stiffness ratio, k_y / k_x, is proportional to n^2 for large n. Values for the stiffness ratio can be approximated by the square of the spring length divided by spring width, $(L / b)^2$, for $b >> 3\tilde{a}$. Decreasing k_y alleviates buckling due to residual stress in the fixed-fixed suspension. However, decreasing the stiffness ratio can adversely affect the stability in comb-drive resonators.

Values calculated from the meander spring-constant expressions are compared with finite-element calculations in Figure 3. The fixed parameters are: $E =$ 165 GPa, $\nu = 0.3$, $w_a = w_b = t = 2$ µm, $n = 6$, and $a = 10$ µm. The finite element calculations are performed using ABAQUS [9]. Four 3-node quadratic beam elements are used to model each span and connector beam. Spring-constant values obtained from nonlinear finite-element analysis are within 1.6% of the values found from linear analysis, since we restrict the simulation to deflections of 0.1 µm. The finite-element and analytic calculations match to better than 1% for all geometries with sufficiently large span lengths. As the span length is decreased, the flexure spring-constant approaches that of a non-linear fixed-fixed beam suspension. The analytic calculation of k_x for very small span lengths ($b < 2$ µm) underestimates the spring constant by around 5% because axial extensional stress in the flexure is neglected. The analytic calculation of k_y

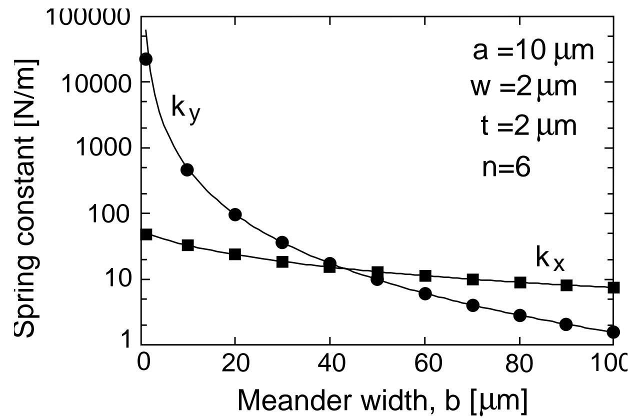

Figure 3. Comparison of analytic meander spring constants (solid lines) with finite-element analysis (points).

for span lengths below 20 µm substantially overestimates the spring constant, also because axial stress is neglected.

C. Meander-Spring Effective Mass

An expression for the ‘effective mass’ of the meander spring in its fundamental vibrational mode is derived by relating the total kinetic energy of the spring in terms of an equivalent lumped mass at the end of an ideal massless spring. A schematic of the first vibrational mode of a meander spring with a guided-end condition is shown in Figure 4(a). The mode shape is approximated by the static mode shape of a displaced guided-end beam of length *L*, as shown by the dotted line in Figure 4(a). Assigning the anchored end of the spring to the origin in the *x*-*y* plane, the expression for the mode shape of the guided-end beam is

$$X(y) = A\left(y^3 - 1.5Ly^2\right) \tag{9}$$

To calculate the total kinetic energy, the meander spring is broken up into discrete S-shaped elements, as shown in Fig. 3(b). Each meander element consists of a span beam, orthogonally connected at both ends to the connector beams of length *a*/2. Each meander element is approximated as having rigid-body translation and rotation components whose magnitudes are linearly related to the mode shape of the guided-end beam. This approximation is valid for sufficient numbers of meanders and small range displacement.

Translation and rotation of each meander element is defined at the center of mass, with *y*-directed translation assumed to be negligible. Therefore, the translational velocity of the ith meander element has an amplitude, $V_x(y)$, proportional to the mode shape at $y = ia$.

$$V_x(y) = \omega_r \left. X\right|_{y=ia} \tag{10}$$

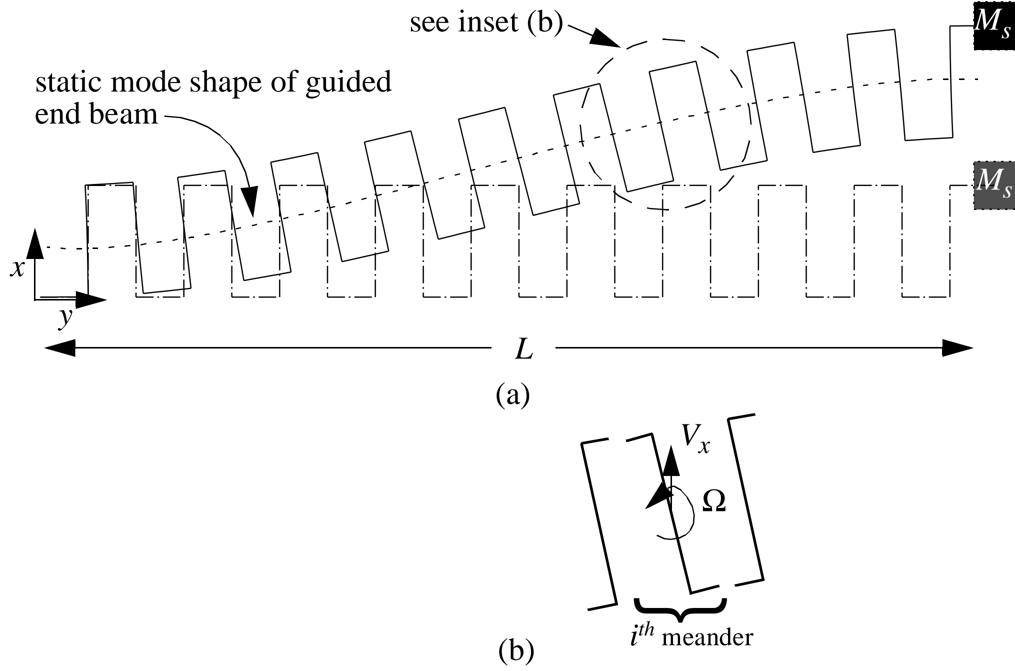

Figure 4. (a) Finite-element simulation of meander spring connected to the shuttle mass, M_s, showing the undisplaced spring (dot-dash lines) and the first vibrational mode shape (solid lines). The overall mode shape is approximated by a guided-end beam mode shape (dotted line). (b) Discretization of meander spring depicting the translation and rotation of the i^{th}meander.

where ω_r is the resonant frequency. Likewise, the amplitude of the rotational velocity, $\Omega(y)$, of the ith meander is proportional to the spatial derivative of the mode shape at $y = ia$.

$$\Omega(y) = \omega_r \left.\frac{dX}{dy}\right|_{y=ia} \tag{11}$$

The maximum kinetic energy of the total mechanical system is

$$KE_{\max} = \frac{1}{2}(M_s + 4\rho hwa)\left.V_x^2\right|_{y=L} + 4\sum_{i=1}^{n-1}\left(\frac{1}{2}m_m \left.V_x^2\right|_{y=ia} + \frac{1}{2}I_m \left.\Omega^2\right|_{y=ia}\right) \tag{12}$$

$$m_m = \rho hw(a+b) \tag{13}$$

$$I_m = \rho hw\left(\frac{b^3}{12} + \frac{ab^2}{2} + \frac{a^3}{12}\right) \tag{14}$$

where m_m and I_m are the mass and the mass polar moment of inertia, respectively, of one meander element, M_s is the shuttle mass, ρ is the density of the polysilicon beam, and h is the beam thickness. The maximum kinetic energy can be rewritten in terms of the effective mass, M_{eff}, of the meander suspension.

$$KE_{\max} = \frac{1}{2}(M_s + M_{\text{eff}})\left.V_x^2\right|_{y=L} \tag{15}$$

where the effective mass is given by

$$M_{\text{eff}} = 4I_m \frac{n^4 - 1}{5L^2 n^3} + 2m_m \frac{78n^6 - 105n^5 + 7n^2 + 20}{105n^5} + 2\rho hwa \tag{16}$$

The fundamental resonance frequency is then found from Rayleigh's method by equating the maximum kinetic energy with the maximum strain energy at resonance. The resonant frequency is given by

$$\omega_r = \sqrt{k_x / (M_s + M_{\text{eff}})} \tag{17}$$

3 Experimental Results

Ten polysilicon microresonators have been fabricated to verify experimentally the analytic expressions for x-directed spring constant and resonant frequency. Each of the resonators has a different meander suspension, labelled A through L. The measured polysilicon thickness is 1.78 µm. The rigid central shuttle is identical for each resonator, and has a mass of approximately 25 ng. Both the comb-finger width and meander beam width are 1.8 µm, and the gap between fingers is 2.2 µm. The theoretical lateral force coefficient is approximately 0.14 nN/V^2, calculated from a two-dimensional finite-element analysis. Table 1 lists the spring parameters for each design. Values for k_x and k_y/k_x are calculated from eqns (5) and (6) using the measured beam thickness and width, and an assumed value of Young's modulus for polysilicon of 165 GPa.

Lateral resonant frequency from analytic calculations, finite-element analysis, and measurements are compared in Figure 5 and the values are listed in the

Table 1. Data for the ten experimental meander-suspension microresonators, labelled A through L

	n	a [µm]	b [µm]	k_x eqn (5) [N/m]	k_y/k_x	f_r eqn (17) [Hz]	f_r (FE) [Hz]	$f_r \pm \sigma$ (measured) [Hz]
A	10	63	81	0.0146	28	3040	3032	2697 ± 183
B	10	65	64	0.0150	45	3143	3137	3172 ± 55
C	10	37	47	0.0727	29	7379	7376	7548 ± 347
D	10	38	37	0.0757	46	7633	7635	8133 ± 342
E	20	27	63	0.0148	42	2908	2899	3348 ± 799
F	20	29	50	0.0145	72	2954	2947	2952 ± 159
G	20	16	37	0.0715	43	7057	7053	7213 ± 372
H	20	17	29	0.0722	73	7242	7243	7325 ± 375
I	10	22	28	0.345	29	17007	17029	17870 ± 833
L	20	10	17	0.356	74	17101	17130	17760 ± 724

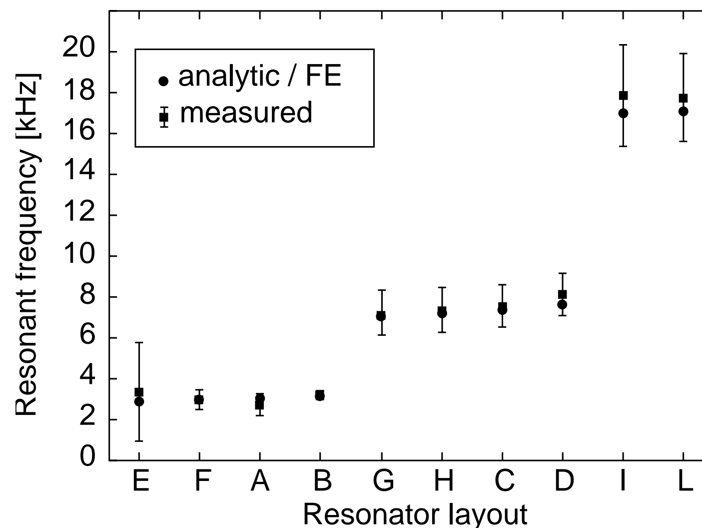

Figure 5. Resonant frequency for the ten microresonator layouts comparing analytic and finite-element (FE) data with measured data. The layouts are presented in increasing resonant frequency. Error bars on the measured data represent $\pm 3\sigma$ variation across the wafer.

last three columns of Table 1. The analytic resonant frequency values found from eqn (17) agree to within 0.3% of the finite-element values and are plotted as a single data point on the figure. Resonant frequency is measured for three devices of each resonator design to obtain the average and standard deviation values in the last column of Table 1. The large standard deviation in resonant frequency is due to the variation in beam width across the wafer. Calculated resonant frequency values are within 13% of the average measured values for all resonators except for the resonator with the largest meanders (A). The calculated frequency of resonator A is well within 3σ of the measured value, however. Neglecting the spring effective mass is a particularly bad approximation for resonators A, B, E, and F, since the total beam length of each spring is greater than 0.5 mm. Residual stress in the film has less than 1% effect on the spring constants or resonant frequency of these structures, based on finite-element simulations.

4 Conclusions

The set of analytic expressions for meander spring constants and effective mass provides a rapid analysis of static and resonant behavior of meander-spring microresonators. The 1% accuracy of the analytic models is much better than the typical accuracy with which thin micromechanical beams can be fabricated. Therefore, the models can be used to relate physical design and process tolerances to micromechanical performance specifications. However, the limits of validity for these models still needs to be explored. Future work includes development of spring-constant models for other spring geometries and for boundary conditions other than the guided-end condition.

Acknowledgments

The authors thank Professor Roger T. Howe and the University of California at Berkeley Microfabrication Laboratory for use of their facilities in fabricating the microresonators. Special thanks to David Loconto for fabrication assistance. This work is funded in part by ARPA.

References

1. Zhang, X. & Tang, W.C., "Viscous air damping in laterally driven microresonators," pp. 199-204, *Proceedings of the IEEE Micro Electro Mech. Syst. Workshop*, Oiso, Japan, 1994.
2. Johnson, W.A. & Warne, L.K., "Electrophysics of micromechanical comb actuators," *J. of Microelectromechanical Systems*, 1995, **4**, 49-59
3. Nguyen, C.T.-C. & Howe, R.T., "CMOS micromechanical resonator oscillator," pp. 199-202, *Technical Digest of the IEEE Int. Electron Devices Meeting*, Washington, D.C., 1993.
4. Z. L. Zhang, G.A. Porkolab, and N. C. MacDonald, "Submicron, movable gallium arsenide mechanical structures and actuators," pp. 72-77, *Proceedings of the IEEE Micro Electro Mech. Syst. Workshop*, Travemunde, Germany, 1992.
5. Fedder, G.K. & Howe, R.T., "Integrated testbed for multi-mode digital control of suspended microstructures," pp. 145-150, *Technical Digest of the Solid-State Sensor and Actuator Workshop*, Hilton Head, SC, 1994.
6. V. P. Jaecklin, C. Linder, and N. F. de Rooij, "Optical microshutters and torsional micromirrors for light modulator arrays," pp. 124-127, *Proceedings of the IEEE Micro Electro Mech. Syst. Workshop*, Fort Lauderdale, FL, 1993.
7. Tang, W.C., Nguyen, T.-C.H., & Howe, R.T., "Laterally driven polysilicon resonant microstructures," *Proceedings of the IEEE Micro Electro Mech. Syst. Workshop*, Salt Lake City, Utah, 1989.
8. Timoshenko, S.P. & Gere, J.M., *Mechanics of Materials*, 2nd ed., Wadsworth, Belmont, 1984.
9. *ABAQUS User's Manual,* Version 5.2, Hibbitt, Karlsson & Sorenson, Inc., Pawtucket, R.I., 1992.